

FABRY-PEROT VERSUS SLIT SPECTROPOLARIMETRY OF PORES AND ACTIVE NETWORK. ANALYSIS OF IBIS AND HINODE DATA

PHILIP G. JUDGE

High Altitude Observatory, National Center for Atmospheric Research, P.O. Box 3000, Boulder CO 80307-3000, USA; judge@ucar.edu

ALEXANDRA TRITSCHLER, HAN UITENBROEK

National Solar Observatory/Sacramento Peak, P.O. Box 62, Sunspot, NM-88349, U.S.A.; ali@nso.edu, huitenbroek@nso.edu
INAF – Osservatorio Astrofisico di Arcetri, I-50125 Firenze, Italy; kreardon@arcetri.astro.it, gcauzzi@arcetri.astro.itKEVIN REARDON, GIANNA CAUZZI AND AND
ALFRED DE WIJN

High Altitude Observatory, National Center for Atmospheric Research, P.O. Box 3000, Boulder CO 80307-3000, USA; dwijn@ucar.edu

ABSTRACT

We discuss spectropolarimetric measurements of photospheric (Fe I 630.25 nm) and chromospheric (Ca II 854.21 nm) spectral lines in and around small magnetic flux concentrations, including a pore. Our long-term goal is to diagnose properties of the magnetic field near the base of the corona. We compare ground-based two-dimensional spectropolarimetric measurements with (almost) simultaneous space-based slit spectropolarimetry. We address the question of noise and cross talk in the measurements and attempt to determine the suitability of Ca II measurements with imaging spectropolarimeters for the determination of chromospheric magnetic fields. The ground-based observations were obtained May 20, 2008, with the Interferometric Bidimensional Spectrometer (IBIS) in spectropolarimetric mode operated at the Dunn Solar Telescope (DST) at Sunspot, New Mexico. The space observations were obtained with the Spectro-Polarimeter of the Solar Optical Telescope (SOT) aboard the Japanese *Hinode* satellite. The agreement between the near-simultaneous co-spatial IBIS and *Hinode* Stokes-*V* profiles at 630.25 nm is excellent, with *V/I* amplitudes compatible with to within 1%. The IBIS *QU* measurements are affected by residual crosstalk from *V*, arising from calibration inaccuracies, not from any inherent limitation of imaging spectroscopy. We use a PCA analysis to quantify the detected cross talk. *QU* profiles with *V* crosstalk subtracted are in good agreement with the *Hinode* measurements, but are noisier owing to fewer collected photons. Chromospheric magnetic fields are notoriously difficult to constrain by polarization of Ca II lines alone. However, we demonstrate that high cadence, high angular resolution monochromatic images of fibrils in Ca II and H α , seen clearly in IBIS observations, can be used to improve the magnetic field constraints, under conditions of high electrical conductivity. Such work is possible only with time series datasets from two-dimensional spectroscopic instruments such as IBIS, under conditions of good seeing.

Subject headings: Sun: photosphere, chromosphere, magnetic fields, spectropolarimetry

1. INTRODUCTION

This is first of several planned papers attempting to derive chromospheric magnetic structure using imaging spectropolarimetry, a new tool with considerable potential. Our motivation is to constrain the magnetic free energy in the solar atmosphere, the cause of many of the Sun's most interesting observable phenomena, yet measurements of this free energy are notoriously difficult to obtain. Line-of-sight (LOS) components of photospheric magnetic fields have been measured using circularly polarized light routinely for over 50 years. Such measurements set no constraints on the free magnetic energy. It was not until credible measurements of the full polarization vector became available (Baur et al. 1980) that the *free* component of the magnetic energy became something amenable to observation.

But several difficulties arise. The magnetic virial theorem relates the total magnetic free energy in a volume overlying a surface to the vector field measured at that surface, provided the surface is in a force-free state (e.g. Low & Lou 1990). Most vector field measurements are made in photospheric lines where, out-

side of sunspot umbrae, the fields are far from force-free. Thus one must either extrapolate the field into the overlying atmosphere, or make measurements higher in the atmosphere where the field is close to force-free (the ratio of gas to magnetic pressure, plasma β , $\ll 1$). The first option has been pursued by many researchers with mixed success (Schrijver et al. 2008; Wiegmann et al. 2008; De Rosa et al. 2009), in essence because the problem is non-linear (Sakurai 1979), is usually cast into force-free form incompatible with photospheric conditions, and is also ill-posed (sensitive to boundary conditions, Low & Lou 1990).

In this paper we begin pursuit of the second option using an imaging spectropolarimeter to observe chromospheric lines. Previous polarimetric studies of chromospheric lines have been successful in recovering magnetic fields (e.g. Metcalf et al. 1995; Solanki et al. 2003; Socas-Navarro 2005; Harvey 2006; Centeno et al. 2006; Pietarila et al. 2007), but are based on slit spectroscopy. As we will show, imaging spectropolarimetry is especially suited to studying the chromosphere because it has the spatial coverage and high temporal cadence needed to

follow dynamic fibril motions which mostly dominate the upper chromosphere (e.g. Judge 2006). Such work is difficult with conventional slit spectrographs. Outside of very quiet regions of the Sun, the plasma β is certainly < 1 in the upper chromosphere, as can be seen by inspection of $H\alpha$ spectroheliograms (e.g. Kiepenheuer 1953; Athay 1976) dominated by fibril structures resulting from the entrainment of plasma by strong magnetic fields. By using measurements of the chromospheric vector field

- the magnetic free energy in the overlying corona follows directly from the virial theorem;
- extrapolations into the overlying atmosphere can be made using a boundary condition which is itself force-free, unlike the photospheric case;
- the change in regime from a forced (photospheric) to force-free state (upper chromosphere and corona) can be probed.

The third point is of more than academic interest. Recent work by Leake & Arber (2006); Arber et al. (2007) has shown that ion-neutral collisions damp components of the current density $\mathbf{j} = \text{curl } \mathbf{B}$ which are perpendicular to the magnetic field \mathbf{B} . A significant component of the free energy is thus dissipated in the chromosphere before it reaches the corona.

Below, we present vector polarimetry of the photosphere (Fe I 630.25 nm) and chromosphere (Ca II 854.21 nm) using the imaging spectropolarimeter IBIS (Cavallini 2006; Reardon & Cavallini 2008). However, while proven for earlier instruments (e.g., the Imaging Vector Magnetograph IVM, Mickey et al. 1996), the technique needs to be proven for IBIS, and so we combine the IBIS data with (nearly) simultaneous measurements of the same Fe I line from the slit spectropolarimeter aboard the *Hinode* satellite, to assess the spectropolarimetric capabilities of IBIS. Later work will present a physical analysis of these data together with $H\alpha$, EUV, X-ray and G band data obtained simultaneously.

2. OBSERVATIONS

Joint observations with the Dunn Solar Telescope (DST), *Hinode*, and TRACE were obtained from 13 to 21 May 2008. Only data from 20 May 2008 were of sufficient quality to merit further study and are reported here. We targeted the strongest magnetic features on the solar disk, but only small pores were observed. Two regions were observed: the first (NOAA 10996), centered near solar latitude and longitude N8.7, E10.2, was also observed by *Hinode*. The second (NOAA 10994, S12.4, W46.1) was observed only at the DST.

Table 1 summarizes the observations. The heliographic pointings listed between instruments were determined from a SOLIS full disk magnetogram. The SOLIS scan was obtained between 15:11:27 and 15:23:23 UT, the region shown in Figure 1 being observed by SOLIS near 15:16:15 UT over a period of 1 minute. The figure shows the context of the NOAA 10996 IBIS and *Hinode* spectropolarimetric measurements, in a SOLIS 630.2 nm magnetogram and a TRACE 19.5 nm image. TRACE 160 nm data obtained at 15:11 UT were used to determine the co-alignment with the SOLIS magnetogram, by eye. The SOLIS-TRACE alignment is accurate to

$\pm 1''$. The 19.5 nm data shown have been corrected for the 160-19.5 nm offset using standard SolarSoft TRACE software, and are from 15:12 UT. Note that relative inter-instrument co-registration can be made at sub-arcsecond scales, smaller than the uncertainties in absolute heliographic coordinates.

It can be seen that only the upper half ($\approx 40'' \times 40''$) of the IBIS field of view (FOV) overlapped the *Hinode* SP FOV. It is also clear that IBIS observed a region predominantly of negative polarity following some $50''$ behind a positive polarity region. These small concentrations of magnetic flux are connected by relatively short coronal loops seen in the 19.5 nm TRACE data. There is some 19.5 nm “moss” emission associated with the photospheric field concentrations. Moss is the bright foot-point emission at the base of an overlying hotter corona (Fletcher & de Pontieu 1999; Berger et al. 1999).

2.1. Spectropolarimetric Observations from IBIS

The IBIS observations reported here were obtained between 14:29 and 15:19 UT. IBIS is a Fabry-Pérot based filtergraph in a classical mount with a circular FOV of diameter $80''$, rapidly tunable in wavelength (Cavallini 2006; Reardon & Cavallini 2008). IBIS was operated in dual-beam spectropolarimetric mode (Tritschler et al. 2009) in which two liquid crystal variable retarders (LCVRs) are placed in a collimated beam in front of the instrument, and a polarizing beam-splitter is inserted in front of the detector. The FOV is then reduced to $\approx 40'' \times 80''$, because the beam splitter produces a pair of simultaneous $I + S_i$ and $I - S_i$ images with $S_i = \text{Stokes } Q, U \text{ or } V^1$. At each wavelength six modulation states were acquired sequentially, with the first beam acquired in the following order: $I + Q$, $I - V$, $I - Q$, $I + V$, $I - U$, and $I + U$. This sampling order was chosen to maximize the efficiency of the LCVR modulation. The Fe I, Ca II and $H\alpha$ lines were sampled with 14, 21 and 22 non-equidistant wavelength points, respectively. In $H\alpha$ only unpolarized measurements were acquired. Thus, a full sequence consists of $(14 + 21) \times 6 + 22 = 232$ exposures, requiring 70 s in total. For the Fe I 630.2 nm and Ca II 854.2 nm lines the scanning was performed by jumping sequentially between the blue and red sides of the line. To avoid detector saturation the exposure time for each individual image was set to 50 ms, which limits the polarimetric sensitivity obtainable. The instrument performed electronic 2×2 binning prior to writing to disk which resulted in a detector image scale of $0.16 \text{ arcsec pixel}^{-1}$.

The narrowband observations are supplemented with simultaneous wide band data (WB, 721 nm) covering the same FOV with a detector image scale of $\sim 0.08'' \text{ pixel}^{-1}$. The WB data were used for alignment purposes and the correction of the effects of anisoplanatism (to first order) during scanning via a de-stretch algorithm using speckle reconstructed WB images as reference images. The speckle reconstructions were calculated from bursts of 77 images each (burst durations of 23 s) using the implementation by Wöger et al. (2008). G-band data covering a FOV of twice the width but the same height as

¹ We will interchangeably use the notations \mathbf{S} , ($IQUV$) and (S_0, S_1, S_2, S_3) as convenient henceforth, to describe the Stokes vector and its components.

the WB data were also obtained at a cadence of 0.2 s on a 1024×1024 detector with $\approx 0.09''$ pixel $^{-1}$. These data are not discussed here. All observations were performed in conjunction with the high-order adaptive optics (AO) system (Rimmele 2004). Seeing conditions were good but variable. Full calibration data sets including flats, darks, resolution targets and polarization calibration measurements were obtained before and after science observations.

The IBIS $I \pm S_i$ data frames were reduced following procedures described by Cauzzi et al. (2008), including dark subtraction, flat fielding, co-alignment with WB images, a blueshift correction needed because of the classical etalon mountings, de-stretching, and co-registration of all images in each sequence. The reduced $I \pm S_i$ frames were then combined and corrected for instrumental polarization to determine the solar Stokes vector \mathbf{S} . The telescope calibration data used were from February 2007. A more recent calibration dataset was acquired in October 2008, but the results were not ready at the time of writing. The measured \mathbf{S} is in a frame of reference defined by the elevation mirror of the telescope (see e.g. Skumanich et al. 1997; Beck et al. 2005). In the solar reference frame (Q positive in the E-W direction on the Sun) a final rotation in the $Q - U$ plane is required. However, prior to this rotation some care is needed because residual crosstalk from V to Q and U is evident in the data. Thus an empirical correction to QU using the V data was applied, as described below, to try to derive the actual QU entering the telescope, before applying the rotation. The appendix describes the different origins of crosstalk in IBIS and the *Hinode* SP.

For the first target, 30 IBIS scans of 70 s each were completed, for the second, just 5 scans were obtained before clouds intervened. Figure 2 shows typical IBIS filtergrams of NOAA 10996 taken in the blue wing of Fe I, Ca II and H α , at the nominal line core position of Ca II and H α , and a magnetogram constructed by subtracting $V(+56$ mÅ) from $V(-74$ mÅ) for the Fe I line. The seeing was examined using a $10''$ square region centered near ($-150'', 120''$), free of measurable magnetic influences. Figure 3 shows the rms intensity contrast measured with IBIS and the *Hinode* SP in the continuum near 630 nm, as a fraction of the mean intensity. Also shown is the 630 nm continuum rms contrast corresponding to $1''$ resolution derived by Lites (2002). The AO-corrected rms contrast was variable, and so was not dominated by stray light. The seeing was clearly worse during the first and 16th-24th IBIS scans. The seeing-limited resolution of these IBIS observations, at best, corresponds to somewhere between $1''$ and the resolution of *Hinode* SP. (Note that “resolution” of *Hinode* here refers to the characteristic width of the point spread function, PSF, modified by the pixel size. In terms of granular contrast statistics, the smaller *Hinode* SP PSF corresponds to an effective resolution close to $0''.315$.)

2.2. Spectropolarimetric Observations from *Hinode*

The Spectro-Polarimeter (SP, Lites et al. 2001) aboard *Hinode* (Kosugi et al. 2007) obtained “fast maps” of the 630 nm region. In typical operation mode, 112 wavelength samples of the SP CCD detector are read, each pixel having a spectral width of 0.00215 nm and a width along the slit of $0.16''$ (Centeno et al. 2009). The 12-

micron wide SP slit presents an effective width of $0.16''$ to the solar image. The fast map mode reduces telemetry volume via an effective 2x2 binning of the image produced by the SP mapping process: the image pixel wells are binned in the direction along the slit during each read of the spectral/spatial CCD image, then successive integrations of one full rotation (1.6 sec) of the retarder polarization modulator are summed onboard. Successive integrations correspond to one step of the image perpendicular to the CCD slit: an average step size of $0.149''$. To further reduce the overall SP data rate for these coordinated observations as a consequence of the failure in late 2007 of the *Hinode* onboard X-band telemetry system (Shimizu 2009), one of the two CCD polarimetry images was not downlinked, and for the remaining data, we retained only the central half of the full $164''$ length of the SP CCD along the slit. The resulting SP fast maps for these observations were then 335×256 pixels, or approximately $99.6'' \times 81.9''$. These maps required ≈ 21 minutes to execute, and have an effective (square) pixel aperture of about $0.3''$. With the *Hinode* rotating retarder modulator, demodulation was accomplished via onboard summing of images corresponding to 4 phases over a half-rotation of the modulator. The Stokes vector was derived using the level 1 data product from the *Hinode* project which includes the 630.15 nm and 630.25 nm lines of Fe I.

While the SP observations are seeing-free, they do experience spacecraft jitter. The amplitude of the jitter is remarkably small ($1\sigma < 0.01''$, Shimizu et al. 2008), which has two implications. First the images are far more stable than can be obtained from the ground. Second, the influence of jitter on the spectropolarimetry is small, when we understand jitter to have the same effect as “seeing” in the sense modeled by Lites (1987); Judge et al. (2004). This issue is reviewed in the Appendix.

3. ANALYSIS

IBIS obtains narrow-band 2D images but must scan through multiple wavelengths to build up the spectra; the SP obtains spectra along the slit but must scan spatially perpendicular to the slit, to build up maps of the solar surface. The instruments also differ in the way the *polarimetry* is performed. IBIS is a “Stokes definition polarimeter”, i.e. during the IBIS integrations only $I + S_i$ for $S_i = QU$ or V is acquired. Other than inevitable $I \rightarrow S_i$ crosstalk, which is mostly removed by the dual beam, there is no other “seeing induced crosstalk”. The combined modulation/demodulation matrices ($\hat{H}'_{ri}(\nu)$ of Lites 1987) are diagonal. Yet such a polarimeter is still susceptible to cross-talk because the telescope mixes the four polarization states prior to entering the polarimeter in a fashion which may be imperfectly calibrated, and the modulation/demodulation is not perfect. Crosstalk induced by calibration errors varies far more slowly than seeing, and could be “calibrated out” if accurate calibration data were available. Difficulties arise because the calibration matrices are imprecisely known. Below, we will apply a simple correction for the $V \rightarrow QU$ crosstalk by simply requiring the average QU profiles to be symmetric around line center. The SP data show this to be a good assumption.

Every SP exposure is a linear combination of I and at least two other Stokes parameters. Such measure-

ments have significant off-diagonal $\tilde{H}'_{ri}(\nu)$ terms. The SP is therefore subject to the systematic errors induced by “seeing-induced crosstalk” (again, for the SP, “image motion” means jitter). But the residual image motion is very small: the factor β_i in Lites’ (1987) formula (15) is far less than it would have been if observing with the SP through the atmosphere. It is in this sense that we can use the SP data as fiducial values against which we compare the data from IBIS.

3.1. Polarization of Fe I 630.2 nm

In Figure 4, direct comparisons of Stokes parameters between IBIS and *Hinode* SP are shown. These data are typical of the entire dataset. The intensity images and magnetograms show the context of the Stokes parameters shown in the rightmost panels, which for the IBIS data shown were extracted from the near-vertical line representing the position of the SP slit. First consider the Stokes IV profiles. The spatial variation of Stokes I, V profiles along the SP slit position is remarkably similar in the two instruments. The higher angular and spectral resolution of the *Hinode* observations is evident. Closer scrutiny reveals that Stokes V to continuum intensity ratios, V/I_c , measured by *Hinode* are larger than those from IBIS, by a factor of typically 2.4. These differences can arise primarily because the magnetic field is spatially intermittent and not fully resolved. Consider V/I_c which measures the net LOS flux per unit area in each resolution element, in the weak field limit of the Zeeman effect (e.g. Lites 2000). This approximation not wildly incorrect for these data. Consider just one magnetic element of area a and LOS field strength B_{los} . The magnetic field generates an intrinsic V_{actual} . But when measured by an instrument i integrating over area $A_i \geq a$, the Stokes V is diluted by the (instrument-dependent) “filling factor” $f_i = a/A_i \leq 1$. Then for instrument i , V/I_c is

$$V_i/I_c \propto f_i B_{los}, \quad (1)$$

Thus the lower the resolution (larger A_i), the smaller the V/I_c signal, when the magnetic field is not resolved. The presence of unpolarized stray light can also reduce V/I_c , but this effect is clearly smaller judging by the measured granular contrast variations. Similar arguments apply to QU data. The data then suggest that the IBIS V profiles sample areas $\lesssim 2.4$ times those sampled by the *Hinode* SP instrument, thus the effective resolution of these IBIS observations is $\lesssim 1.5\times$ worse than that of *Hinode*. Taking, as noted above, the latter to be $0''.3$ (and not twice this which is the Nyquist limit), we get $0''.49$ for IBIS. This number is compatible with the seeing-limited resolution derived independently from Figure 3. Furthermore, the Stokes V/I_c integrated over unipolar areas of several Mm^2 observed by IBIS and *Hinode* SP give the same LOS magnetic flux (not flux density) to within 1%, validating the above analysis, no unresolved flux of opposite sign being significant. Below, we will show that the IBIS and *Hinode* Stokes V data, as reduced into principal components, have very similar leading order eigenvectors.

IBIS QU profiles are shown twice in Figure 4. Those marked “Orig.” are profiles obtained in the telescope reference frame. These data are clearly not symmetric about line center, and appear V -like throughout. Rotation of these profiles alone to the solar reference

frame only involves linear combinations of the QU data which will yield similar profiles with large asymmetric, V -like components. The entire dataset is similarly contaminated by V -like profiles. Some extra retardance has not been accounted for in the telescope calibration which converts incoming V to QU before entering the polarimeter. Requiring that QU be symmetric about the (Doppler-shifted) line centers, we found that the sign and amount of $V \rightarrow QU$ crosstalk is not a strong function of time, position on the detector etc.. Thus this crosstalk can be accounted for by a fixed Mueller matrix, of which the important components lead to the corrections:

$$Q = Q(Orig) - (0.085 \pm 0.004)V, \text{ and}$$

$$U = U(Orig) - (0.051 \pm 0.003)V,$$

using 1σ statistical uncertainties. Figure 4 shows these corrected QU profiles also rotated to the solar reference frame. The agreement with *Hinode* SP data for QU is now remarkable. These corrections are just the largest terms arising from extra retardance 6° oriented at about 30° to the IBIS reference direction, in which QUV become mixed via the Mueller algebra (e.g. Seagraves & Elmore 1994). This retardance appears to arise from a thin film of oil noted on the exit port of the telescope. The corrections above were applied to the lines of both Fe and Ca.

The *Hinode* SP data for QU in the magnetic network and pore are significantly above the designed sensitivity limit of the instrument. They have essentially the symmetric profiles expected from the Zeeman effect. The heritage of *Hinode*’s SP is in the Advanced Stokes Polarimeter (Elmore et al. 1992; Skumanich et al. 1994) and Diffraction Limited Polarimeter (Sankarasubramanian et al. 2006). Such profiles are clearly of solar origin (e.g. Lites 2000) and free of large systematic errors introduced, for example, by the seeing-induced $V \rightarrow QU$ (Lites 1987; Judge et al. 2004).

3.2. Polarization of Ca II 854.2 nm

Figure 5 shows a comparison of Fe I and Ca II profiles for NOAA 10996, plotted as in figure 4, and from the same pixels. At the peak of the V profile near $y = 179''$ the signal-to noise ratio of V is ~ 7 for the Ca II data shown. No significant QU signal was detected in the Ca II data. These data differ qualitatively from those of Fe I, as found from the analysis of Fe I 849.7 and 853.8 nm lines observed with SPINOR by Pietarila et al. (2007). Beyond 0.04 nm from line center, i.e. at wavelengths where at least the intensity is formed in the upper photosphere (Cauzzi et al. 2008), the Ca II V profiles are similar to those of Fe I in their signs and spatial distribution along the slit. Thus the nominal calibration of IBIS leads to credible Stokes V signals in the parts of the Ca II line profiles whose intensities originate in the upper photosphere. Hence, the (stronger) Stokes V signals in the cores are also credible signals, formed in the chromosphere. Within 0.04 nm of the line core, the profiles are spatially much more diffuse, reflecting an expansion of magnetic flux with height, but the core profiles themselves are more complex than their photospheric counterparts.

The “magnetograms” in the second column are constructed by subtracting the blue lobes of each line’s V

profile from the red lobes, taking no account of Doppler shifts, at ± 0.0064 and ± 0.017 nm from line center for Fe I and Ca II respectively. V profiles show that Ca II “magnetograms” are a mix of Doppler, thermal and magnetic signals which cannot be interpreted straightforwardly in terms of LOS components of the chromospheric magnetic field. Nevertheless chromospheric magnetic fields are the origin of Stokes V in Ca II in this region, but there are also large influences from NLTE radiative transfer and chromospheric dynamics (Pietarila et al. 2007). In particular, the Ca II line *intensity* forms over many scale heights (e.g., see figure 5 of Cauzzi et al. 2008). Hence the inner wings form in the upper photosphere where the magnetic field is relatively strong (compare the Fe I line core data with the Ca II line wing data in Figure 2). But the core (within roughly ± 0.02 nm of line center) forms some 1Mm (6-7 pressure scale heights) higher, in the middle to upper chromosphere. The core intensity data (see also figure 4 of Cauzzi et al. 2008) are dominated by magnetically-dominated fibril structures, over concentrations of photospheric magnetic flux. The question of the formation heights of Stokes V for the Ca II 854.2 nm line in such regions is complex, and will be addressed in later work. For now we simply note that contributions to V can arise from the bulk of the chromosphere, spanning several pressure scale heights and including the plasma $\beta = 1$ surface. Also the V profiles below $y = 178$ have two peaks and are correlated with strong line core emission, but that from $y = 179$ to 184 the V profile is simpler and the cores are dark. Evidently the relationship between bright Ca II emission and magnetic field is not linear in our data. Similar results have been reported elsewhere (e.g. Socas-Navarro et al. 2006).

Calibrated data for NOAA 10994 are shown in Figure 6, including profiles extracted from two columns (“a” and “b”). The local vertical of this region is at 47° to the LOS, thus strong vertical fields are seen partially as QU signals from the transverse Zeeman effect, as well as V . Credible QU profiles are observed in the Ca II 854.2 nm line as well as the Fe I 630.2 nm line. These show perhaps some residual V to QU crosstalk. This is not surprising given the difference in wavelength between the Fe I and Ca II lines and the unknown optical properties of the oil film.

3.3. Principal Components

Principal Component Analysis (PCA), a pattern/shape recognition method, is useful in application to solar Stokes profiles because principal components (PCs) are often directly related to underlying atmospheric parameters (Skumanich & López Ariste 2002), for example to magnetic field strength, direction, line of sight motions, and thermal properties. Here we use it also to quantify crosstalk. PCs are the eigenvectors of the covariance matrix with components defined as

$$C_{ij} = \langle S_i S_j \rangle_{\mathbf{x}, t}, \quad (2)$$

where S_i is the Stokes vector component (one of $IQUV$) at wavelength i , and the angle brackets imply an average over all spatial pixels \mathbf{x} and/or time t . Denoting e_i as the i^{th} eigenvalue of C and $v_{i,j}$ as the j^{th} component of the eigenvector belonging to e_i , any data point $d_{k,j}$, $k =$

spatial and/or temporal index, is represented by

$$d_{k,j} = \sum_{i=1}^{n_\lambda} c_{k,i} v_{i,j} \quad (3)$$

where n_λ is the number of wavelengths, and

$$c_{k,i} = \sum_{j=1}^{n_\lambda} d_{k,j} v_{i,j}. \quad (4)$$

Assume that the eigenvalues/ vectors are ordered in decreasing magnitude. When the eigenvalues e_i drop steeply with increasing i , then most properties of the data are described by the first few eigenvectors in the sum. The data points across the line profiles are not completely independent of one another, and so the data can be represented by truncating the sum to values smaller than n_λ . If however, the spectrum is shallow, there is much independence between data points and a larger number of vectors are needed. In our IBIS data, Stokes IV have steep spectra, but Q and U are shallower. This is because QU are noisy. Noise introduces linear independence between the different wavelengths across the lines, thereby flattening the eigenvalue spectrum.

Figure 7 shows the first three eigenvectors derived for SP and the IBIS dataset obtained near 14:43 UT, covering the FOV shown in 4. The IBIS QU data shown are calibrated but uncorrected for cross talk because our aim is to quantify the cross talk here using PCA. Consider first the QUV data from *Hinode* in the figure. The PCs for *Hinode* Q and U are almost symmetric around the line center and resemble the second derivative of the intensity profile, the principal V component being antisymmetric. This is as expected because the *Hinode* V and QU profiles arise from the first and second order Zeeman effect, respectively. While the IBIS principal V component is asymmetric, so too are the PCs of QU . PCA has thus revealed the previously identified crosstalk in QU as the principal signal, but it is to be noted that the more symmetric second and third eigenvectors have eigenvalues just 0.6 and 0.2 dex below the PC’s eigenvalue. There is therefore significant signal of the appropriate symmetry in these IBIS data: the second PCs of IBIS QU resemble those seen with SP.

Using PCA, $V \rightarrow QU$ cross-talk can be quantified by projection of profiles onto the leading order PCs. Figure 8 shows scatter plots of leading order coefficients c_{k1} for Q and U with those for V , for typical observations k from both instruments. There is no significant correlation for the *Hinode* SP data, but the IBIS coefficients are correlated, the figure lists Spearman rank correlation coefficients. The dashed lines show $c_1(Q) = 0.085c_1(V)$ and $c_1(U) = 0.051c_1(V)$, the numerical coefficients being those of section 3.1. If the QU data were pure cross-talk from an antisymmetric V , then all points would be distributed along the plotted lines. The actual distributions show significant scatter, data for U having a broader, skewed distribution. This behavior, arising from an unknown source of systematic error, highlights the limitation of the simple *post-facto* corrections of section 3.1. The corrected U profiles are probably reliable to at best $\pm 50\%$, given the plotted scatter. Nevertheless, the PCA analysis lends support for our empirical corrections.

PCA should also help disentangle the complex Ca II *QUV* profiles, in terms of identifying the physical parameters most directly related to the Stokes profiles (Skumanich & López Ariste 2002). Figure 9 shows the eigenvalue spectra and first few eigenvectors of the PCA expansion, for a $10'' \times 10''$ area centered on NOAA 10994 (see Figure 6), a region chosen because it has measurable linear polarization in the Ca II 854.2 nm line. The *QU* profiles are mostly dominated by noise (as shown by the shallow gradient in the eigenvalue spectrum, and noisy first eigenvector). But the other eigenvectors show that genuine *QU* signals are present for this small pore. Stokes *V* contains real signal because the first eigenvector is predominantly of asymmetric form, and the eigenvalue spectrum is steeper than *Q* and *U*. This *V* component has no obvious net amplitude or area asymmetry, in contrast with Pietarila et al. (2007), who found a net red-asymmetry in the 854.2 nm line for some active network.

3.4. Fibrils and their motions constrain the magnetic field

Figure 5 also shows core and wing intensities of the H α line from IBIS. The wing and core behavior is similar to the 854.2 nm line of Ca II, reflecting conditions at deeper layers of the photosphere and top of the chromosphere respectively, consistent with the picture of line formation of Athay (1976). The fibril structures in the core intensity images are similar to, not identical with, those for the 854.2 nm Ca II line. H α images at a given wavelength setting of IBIS are remarkably structured. The motions of “blobs” of emission or absorption seem to trace the fibril- and hence magnetic field line- orientations. Curiously, on the red side of H α , blobs appear to converge on the underlying photospheric flux concentrations. On the blue side, they diverge from them. To try to determine if these “blobs” correspond to real material motion, we show in figure 10 H α data from three snapshots in the time series. The leftmost panel is the line core intensity image of the middle snapshot. The three other panels show data using PCA. The particular eigenvector which corresponds to line of sight Doppler shift, i.e. having a profile corresponding to the first derivative of the intensity profile with respect to wavelength, was identified. This component was then projected onto the data themselves at each point and time and images displayed, yielding Doppler maps. (These Doppler velocities are similar to those derived from the first wavelength moment of the profiles). Darker (lighter) profiles correspond to blue (red) shifted components. Examining the region between the two plotted circles, several dark blobs of material move away from the circle centers with time. The Doppler shifts of these blobs are towards the observer ($v_{los} < 0$). (While less clear, movies of the red-shifted material show components converging onto the circle centers). This behavior is compatible with simple flows of absorbing material which diverge from or converge to a magnetic structure originating from the photospheric flux concentration and expanding outwards, perhaps into the corona. Hence, using proper motions (determined by eye in this case) and Doppler shifts, one can trace out the 3D vector velocity field of the entrained fibril material. In the particular blobs shown, the vector velocity has components $(v_x, v_y, v_z) \approx (-7, -7, -3)$ km s $^{-1}$, i.e. the velocity is inclined at 17° to the plane of the sky,

only 16° from the local solar horizontal plane.

These measurements are more than a curiosity. Given the strong collisional coupling between the neutral and ionized components, and the high electrical conductivity, the 3D velocity field traces out the direction of the vector magnetic field, which is therefore also only $\approx 16^\circ$ to the horizontal plane. Such observations offer observers the important opportunity to augment spectropolarimetric measurements of chromospheric vector magnetic fields, which will always suffer from weak Zeeman-induced *QU* signals. Measurement of the LOS component of the magnetic field from Stokes *V*, coupled with kinematic fluid velocities, determines the vector magnetic field. Chromospheric fibril observations in Ca II or H α are thus far richer than suggested by inspection of Figure 5. They will be discussed in the context of constraining the chromospheric magnetic fields elsewhere.

4. DISCUSSION

We have demonstrated the fidelity of a two-dimensional filtergraph instrument, IBIS for accurate Stokes *V* measurements at high angular resolution, by verification through almost simultaneous measurements from the Spectro-Polarimeter on board the *Hinode* satellite. IBIS measurements of Stokes *QU* profiles of the Fe I 630.2 nm line are subject, as expected, to systematic errors (cross talk), which we have quantified both empirically and using Principal Component Analysis. IBIS is a Stokes Definition Polarimeter so that just one polarization state is measured during each camera integration. Therefore, the cross talk among *QU* and *V* is of a slowly varying character, originating from errors in the telescope calibration data. An empirical correction yields *QU* profiles in remarkable agreement with the SP data, yielding credible *QU* profiles both in the Fe I 630.2 nm line, and, for a pore far from disk center at a viewing angle of 47° , credible observations of Stokes *QU* in the chromospheric Ca II 854.2 nm line.

We believe this is the first time that a direct comparison of spectropolarimetry has been made between slit and two-dimensional filtergraph instruments using data of the same region obtained within a few seconds of each other. (The Advanced Stokes Polarimeter had this capability by use of a slit-jaw but the results were not very good - Lites 2009, private communication). Given the intrinsic difficulty of making spectropolarimetric measurements from the ground, the excellent agreement of Stokes profiles found with near-simultaneous observations from IBIS and the *Hinode* SP provides strong support for the credibility of measurements made with an IBIS-like instrument. We note that the magnetic features observed here are rather weak compared with strong sunspots, and the IBIS camera is to be updated to permit a larger duty cycle and increased signal to noise.

Our goal is to diagnose properties of the magnetic field near the base of the corona using, in part, the Ca II chromospheric lines. At face value, the Ca II data appear to be of limited use in that under many conditions the noise is dominant in the *QU* data and corrections must be applied for inaccuracies in the telescope polarization calibration data. Other complications include difficulties concerning non-LTE transfer of in the Ca II lines. Yet IBIS has some significant advantages over slit spectropolarimetric measurements. IBIS images can be corrected

using image reconstruction techniques. This is important because an angular resolution of $1''$ or better, covering fields of tens of seconds of arc with a spectral resolution of some tens of $\text{m}\text{\AA}$ is required to see clearly the fibril structure of the upper chromosphere (see Figure 2). A cadence of 70 seconds is barely enough to track kinematic motion along the fibrils, $\lesssim 20$ seconds being highly desirable. Such criteria may not be achieved using slit instruments. The observation of fibril kinematics, even in unpolarized light, appears important for diagnosing chromospheric magnetic fields because fibrils not only trace out magnetic lines of force, but the partially ionized plasma is required to flow along these lines because of the large electrical conductivity. From our IBIS data for $\text{H}\alpha$, it appears possible to measure the velocity vector of fibril “blobs” in the plane of the sky, and along the LOS, yielding the direction of the magnetic field (to within an ambiguity of 180°). Coupled with the Stokes V signals which may in principle yield the LOS field strength, there is thus hope that the vector magnetic field might be constrained from such observations.

In conclusion, this dataset provides, for the first time, credible imaging spectropolarimetry from photosphere through the chromosphere together with a useful time series of resolved fibril motions in the upper chromosphere. These data can be used to place observational constraints on the vector magnetic field throughout the chromosphere. In the case of NOAA 10996, we have found that the magnetic field is highly inclined to the LOS, as in a traditional magnetic “canopy” (Giovannelli 1982), and that the chromospheric heating rates are not simply related to the Stokes V profiles of Ca II . We will explore the possibilities further using the data described here in later publications. More generally, IBIS holds promise as a tool for chromospheric vector polarimetry in the Ca II 854.2 nm line, following the work on a larger sunspot by Socas-Navarro (2005).

PGJ gratefully acknowledges the help of F. Woeger in speckle reconstruction, and discussions with B. W. Lites whose comments helped to improve the manuscript. Hinode is a Japanese mission developed and launched by ISAS/JAXA, collaborating with NAOJ as a domestic partner, NASA and STFC (UK) as international partners. Scientific operation of the Hinode mission is conducted by the Hinode science team organized at ISAS/JAXA. This team mainly consists of scientists from institutes in the partner countries. Support for the post-launch operation is provided by JAXA and NAOJ (Japan), STFC (U.K.), NASA (U.S.A.), ESA, and NSC (Norway). This research has also made use of NASA’s Astrophysics Data System (ADS). An anonymous referee helped us improve the presentation.

REFERENCES

- Arber T. D., Haynes M., Leake J. E., 2007, *ApJ* 666, 541
 Athay R. G., 1976, *The Solar Chromosphere and Corona: Quiet Sun*, Reidel: Dordrecht
 Baur T. G., House L. L., Hull H. K., 1980, *Sol. Phys.* 65, 111
 Beck C., Schlichenmaier R., Collados M., Bellot Rubio L., Kentischer T., 2005, *A&A* 443, 1047
 Berger T. E., De Pontieu B., Schrijver C. J., Title A. M., 1999, *ApJ* 519, L97
 Cauzzi G., Reardon K. P., Uitenbroek H., Cavallini F., Falchi A., Falciani R., Janssen K., Rimmele T., Vecchio A., Wöger F., 2008, *A&A* 480, 515
 Cavallini F., 2006, *Solar Phys.* 236, 415
 Centeno R., Collados M., Trujillo Bueno J., 2006, *ApJ* 640, 1153
 Centeno R., Lites B. W., de Wijn A. G., 2009, in B. W. Lites, M. Cheung, T. Magara, J. Mariska (eds.), *Second Hinode Science Meeting*, in press
 De Rosa M. L., Schrijver C. J., Barnes G., Leka K. D., Lites B. W., Aschwanden M. J., Amari T., Canou A., McTiernan J. M., Régnier S., Thalmann J. K., Valori G., Wheatland M. S., Wiegmann T., Cheung M. C. M., Conlon P. A., Fuhrmann M., Inhester B., Tadesse T., 2009, *ApJ* 696, 1780
 Elmore D. F., Lites B. W., Tomczyk S., Skumanich A. P., Dunn R. B., Schuenke J. A., Streander K. V., Leach T. W., Clambellan C. W., Hull H. K., Lacey L. B., 1992, *Procs. SPIE* 1746, 22
 Fletcher L., de Pontieu B., 1999, *ApJ* 520, L135
 Giovanelli R. G., 1982, *Solar Phys.* 80, 21
 Harvey J. W., 2006, Vol. 358 of *Astronomical Society of the Pacific Conference Series*, 419
 Judge P., 2006, in J. Leibacher, R. F. Stein, H. Uitenbroek (eds.), *Solar MHD Theory and Observations: A High Spatial Resolution Perspective*, Vol. 354 of *Astronomical Society of the Pacific Conference Series*, 259
 Judge P. G., Elmore D. F., Lites B. W., Keller C. U., Rimmele T., 2004, *Applied Optics: optical technology and medical optics* 43, issue 19, 3817
 Kiepenheuer K. O., 1953, in G. P. Kuiper (ed.), *The Sun*, Chicago University Press, Chicago, p. 322
 Kosugi T., Matsuzaki K., Sakao T., Shimizu T., Sone Y., Tachikawa S., Hashimoto T., Minesugi K., Ohnishi A., Yamada T., Tsuneta S., Hara H., Ichimoto K., Suematsu Y., Shimojo M., Watanabe T., Shimada S., Davis J. M., Hill L. D., Owens J. K., Title A. M., Culhane J. L., Harra L. K., Doschek G. A., Golub L., 2007, *Solar Phys.* 243, 3
 Leake J. E., Arber T. D., 2006, *A&A* 450, 805
 Lites B., 2002, *ApJ* 573, 431
 Lites B. W., 1987, *Applied Optics* 26, 3838
 Lites B. W., 2000, *Reviews of Geophysics* 38, 1
 Lites B. W., Elmore D. F., Streander K. V., 2001, in M. Sigwarth (ed.), *Advanced Solar Polarimetry – Theory, Observation, and Instrumentation*, Vol. 236 of *Astronomical Society of the Pacific Conference Series*, 33
 Low B. C., Lou Y. Q., 1990, *ApJ* 352, 343
 Metcalf T. R., Jiao L., McClymont A. N., Canfield R. C., Uitenbroek H., 1995, *ApJ* 439, 474
 Mickey D. L., Canfield R. C., Labonte B. J., Leka K. D., Waterson M. F., Weber H. M., 1996, *Solar Phys.* 168, 229
 Pietarila A., Socas-Navarro H., Bogdan T., 2007, *ApJ* 663, 1386
 Reardon K. P., Cavallini F., 2008, *A&A* 481, 897
 Rimmele T. R., 2004, in D. Bonaccini Calia, B. L. Ellerbroek, R. Ragazzoni (eds.), *Society of Photo-Optical Instrumentation Engineers (SPIE) Conference Series*, Vol. 5490, p. 34
 Sakurai T., 1979, *PASJ* 31, 209
 Sankarasubramanian K., Lites B., Gullixson C., Elmore D., Hegwer S., Streander K., Rimmele T., Fletcher S., Gregory S., Sigwarth M., 2006, Vol. 358 of *Astronomical Society of the Pacific Conference Series*, 201
 Schrijver C. J., DeRosa M. L., Metcalf T., Barnes G., Lites B., Tarbell T., McTiernan J., Valori G., Wiegmann T., Wheatland M. S., Amari T., Aulanier G., Démoulin P., Fuhrmann M., Kusano K., Régnier S., Thalmann J. K., 2008, *ApJ* 675, 1637
 Seagraves P. H., Elmore D. F., 1994, *Proc. SPIE* 2265, 231
 Shimizu T., 2009, in B. W. Lites, M. Cheung, T. Magara, J. Mariska (eds.), *Second Hinode Science Meeting*, in press
 Shimizu T., Nagata S., Tsuneta S., Tarbell T., Edwards C., Shine R., Hoffmann C., Thomas E., Sour S., Rehse R., Ito O., Kashiwagi Y., Tabata M., Kodeki K., Nagase M., Matsuzaki K., Kobayashi K., Ichimoto K., Suematsu Y., 2008, *Solar Phys.* 249, 221
 Skumanich A., Lites B. W., Martínez Pillet V., 1994, in R. J. Rutten, C. J. Schrijver (eds.), *Solar Surface Magnetism*, 99
 Skumanich A., Lites B. W., Martínez Pillet V., Seagraves P., 1997, 110, 357
 Skumanich A., López Ariste A., 2002, *ApJ* 570, 379

Socas-Navarro H., 2005, ApJ 631, L167
 Socas-Navarro H., Elmore D., Pietarila A., Darnell A., Lites
 B. W., Tomczyk S., Hegwer S., 2006, Solar Phys. 235, 55
 Solanki S. K., Lagg A., Woch J., Krupp N., Collados M., 2003,
 Nature 425, 692
 Tritschler A., Reardon K. P., Wöger F., Uitenbroek H., Tomczyk
 S., Casini R., 2009, in preparation

Wiegmann T., Thalmann J. K., Schrijver C. J., Derosa M. L.,
 Metcalf T. R., 2008, Solar Phys. 247, 249
 Wöger F., von der Lühe O., Reardon K., 2008, A&A 488, 375

APPENDIX

ORIGINS OF CROSSTALK

Consider for simplicity the case of a perfect polarimeter. Let \mathbf{M} be the Mueller matrix describing the known telescope calibration parameters. The Stokes vector \mathbf{S} entering the polarimeter is $\mathbf{R} = \mathbf{M}\mathbf{S}$ where \mathbf{S} is the (desired) solar Stokes vector. \mathbf{R} is inferred from the modulation and analysis of instrument i . Then the estimate of the solar Stokes vector from this instrument is

$$\mathbf{S}^i = \mathbf{M}^{-1}\mathbf{R}$$

With (fictional) perfect knowledge of the Mueller matrix, the solar Stokes vector is

$$\mathbf{S} = \mathbf{M}_0^{-1}\mathbf{R}$$

We can write $\mathbf{M} = \mathbf{M}_0 + \mathbf{E}$ where the (unknown) elements of the error matrix \mathbf{E} are assumed small compared with \mathbf{M}_0 —the telescope calibration matrix is close to the actual matrix. Keeping first order terms only,

$$\mathbf{S} - \mathbf{S}^i = \mathbf{E}\mathbf{M}^{-1}\mathbf{R} \equiv \mathbf{E}\mathbf{S}^i,$$

which is the error in the inferred solar Stokes vector resulting from an inaccurate telescope calibration. Off-diagonal (unknown) terms in \mathbf{E} convert the inferred \mathbf{S}^i values into other Stokes components. For a stable instrument, \mathbf{E} can be considered constant or very slowly varying with time. This kind of error is present in all practical polarimeters.

In the presence of atmospheric seeing, the Stokes vector entering the telescope is a rapidly varying distortion of \mathbf{S} in which neighboring points on the solar surface are spatially smeared. Let $T_\alpha(x, y; t)$ represent the α component of the Stokes vector entering the telescope from apparent position (x, y) on the sky at time t . Then, including just the lowest order (tip/tilt) distortions at any time t , \mathbf{T} arises from a different place on the sky $(x', y') = (x + \delta x(t), y + \delta y(t))$. Expand $T_\alpha(x, y; t)$ as a Taylor series in the solar Stokes component S_α on the sky:

$$T_\alpha(x, y; t) = S_\alpha(x + \delta x, y + \delta y; t) \approx S_\alpha(x, y; t) + \nabla S_\alpha \cdot \mathbf{s}(t)$$

to first order (Judge et al. 2004). Here the ∇ operator and vector $\mathbf{s}(t)$ are vectors in the (x, y) plane, $\mathbf{s}(t) = (\delta x(t), \delta y(t))^T$ is the tip-tilt component of the seeing. Let P_ν be the power spectrum of the seeing. All measurements require a finite integration time τ , during which the seeing $\mathbf{s}(t)$ varies. At all frequencies ν where $P_\nu \tau \geq 1$, seeing detrimentally affects the measurements. When integrated over time τ , detectors record energy

$$\int_0^\tau \sum_{\alpha=0}^3 a_\alpha T_\alpha(x, y; t) dt = \int_0^\tau \sum_{\alpha=0}^3 a_\alpha \{S_\alpha(x, y; t) + \nabla S_\alpha \cdot \mathbf{s}(t)\} dt, \quad (\text{A1})$$

where $a_0 = 1$ ($S_0 = I$) and $a_{\alpha \neq 0}$ depends on the polarimeter's particular modulation and integration scheme. With many realizations of the seeing, the equation becomes

$$\sum_{\alpha=0}^3 a_\alpha \langle T_\alpha \rangle = \sum_{\alpha=0}^3 a_\alpha \langle S_\alpha \rangle, \quad (\text{A2})$$

because $\langle \nabla S_\alpha \cdot \mathbf{s}(t) \rangle$ averages to zero when $\mathbf{s}(t)$, arising from atmospheric turbulence, is statistically spatially symmetric. The $\langle S_\alpha \rangle$ components have variances arising from the seeing:

$$\sigma_\alpha^2 = \langle |\nabla S_\alpha \cdot \mathbf{s}(t)|^2 \rangle \quad (\text{A3})$$

which Lites (1987) has shown can be evaluated from the seeing power spectrum using the assumption that the seeing is a random phenomenon. Equation (A2) is a linear system for the desired solar components $\langle S_\alpha \rangle$ in terms of the measurements $\langle T_\alpha \rangle$, subject to statistical variations described by σ_α .

For a Stokes definition polarimeter like IBIS, $a_{\alpha=1,2,3}$ is non-zero only for one Stokes parameter, β say. Then the above equations relate $\langle S_0 \rangle + a_\beta \langle S_\beta \rangle$ only to $\langle T_0 \rangle$ and $a_\beta \langle T_\beta \rangle$. The second beam yields simultaneous measurements of equation $\langle T_0 \rangle - a_\beta \langle T_\beta \rangle$, and this two equation system is solved for all components S_β in terms of T_α as usual, with uncertainties propagated via σ_0 and σ_β .

But for other polarimeters, like the SP on *Hinode*, a_α is non-zero for at least two of QUV during each measurement. The above equation becomes a system of more than two equations. After eliminating the intensity from the equation using the second beam we see that Stokes parameter S_β is also influenced though the terms $\sigma_{\alpha \neq \beta}$. If the variances σ_α (e.g. Stokes V) are larger than the desired terms S_β (e.g. Stokes Q), then the linear system yields estimates for S_β which are dominated in any particular realization by terms of order σ_α . In words, crosstalk arises because, during

Table 1
Log of observations for 20 May 2008

Observatory	Instrument	Observable	Center	FOV	Time UT
DST	IBIS	Fe I 630.2, Ca II 854.2, H α	(-161,171)	40 \times 80	14:29-15:05
	WL	white light		40 \times 80	ditto
	G band	G band		90 \times 90	ditto
<i>Hinode</i>	SP	Fe I 630.2 fast map	(-144,210)	107 \times 82	14:30-16:39
	FG	Na I D, Ca II H, G band	(-137,204)	82 \times 82	14:30-16:41
	EIS	9 lines	(-126,189)	520 \times 512	14:30-16:37
	XRT	3 bands	(-139,169)	130 \times 169	14:00:16:36
<i>TRACE</i>		WL, 160nm, 19.5nm	(-166,199)	512 \times 512	14:01-16:42
DST	IBIS	Fe I 630.2, Ca II 854.2, H α	(666,-193)	40 \times 80	15:12-15:19
	WL	white light			ditto
	G band	G band			ditto

Note. — Solar coordinates are relative to the SOLIS magnetogram obtained near 15:16 UT and are reliable to about $\pm 1''$. The center of the SP and FG images reported in the headers before 15:05 UT were quite different from those in the table, being (-151,183) and (-145,176) respectively. The *TRACE* image center is for the 19.5 nm band. The IBIS commanded pointing was (-165,158). The pointing is approximate for the EIS instrument.

the exposure for modulation state $S_0 + S_\beta$, fluctuations in time occur in $S_{\beta \neq \alpha}$ resulting from the motion of the solar image with contains structure. The great advantage of the SP is its remarkably small rms image motion, so that image-motion induced cross talk is practically negligible.

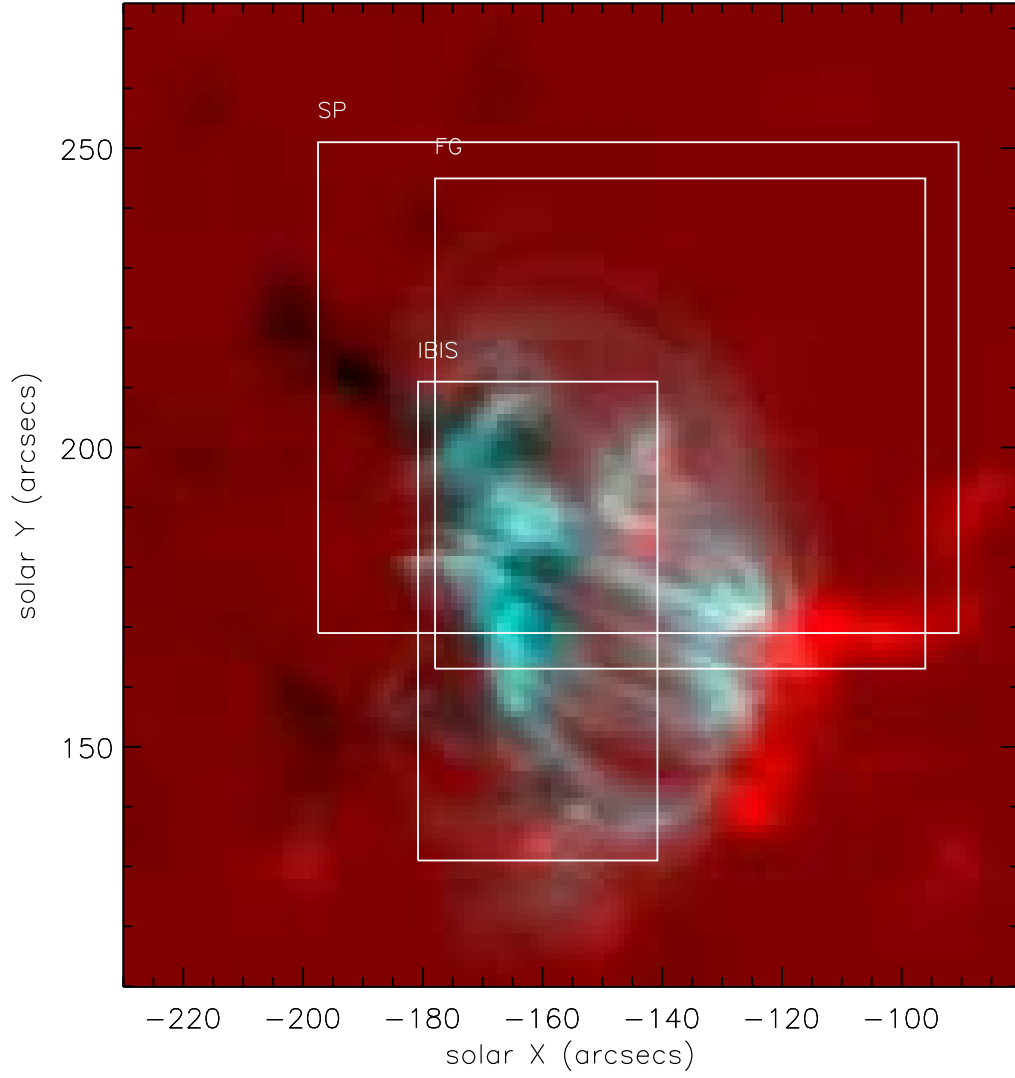


Figure 1. A context image from SOLIS (red) and *TRACE* (cyan) showing the areas observed around NOAA 10996 with the *Hinode* (spectropolarimeter- “SP”, filtergram- “FG”) and with IBIS, before 15:06 UT on 20 May 2008. The SOLIS scan began at 15:11 UT, the *TRACE* image shown was obtained at 15:12 UT. The image coordinates refer to the SOLIS coordinate system.

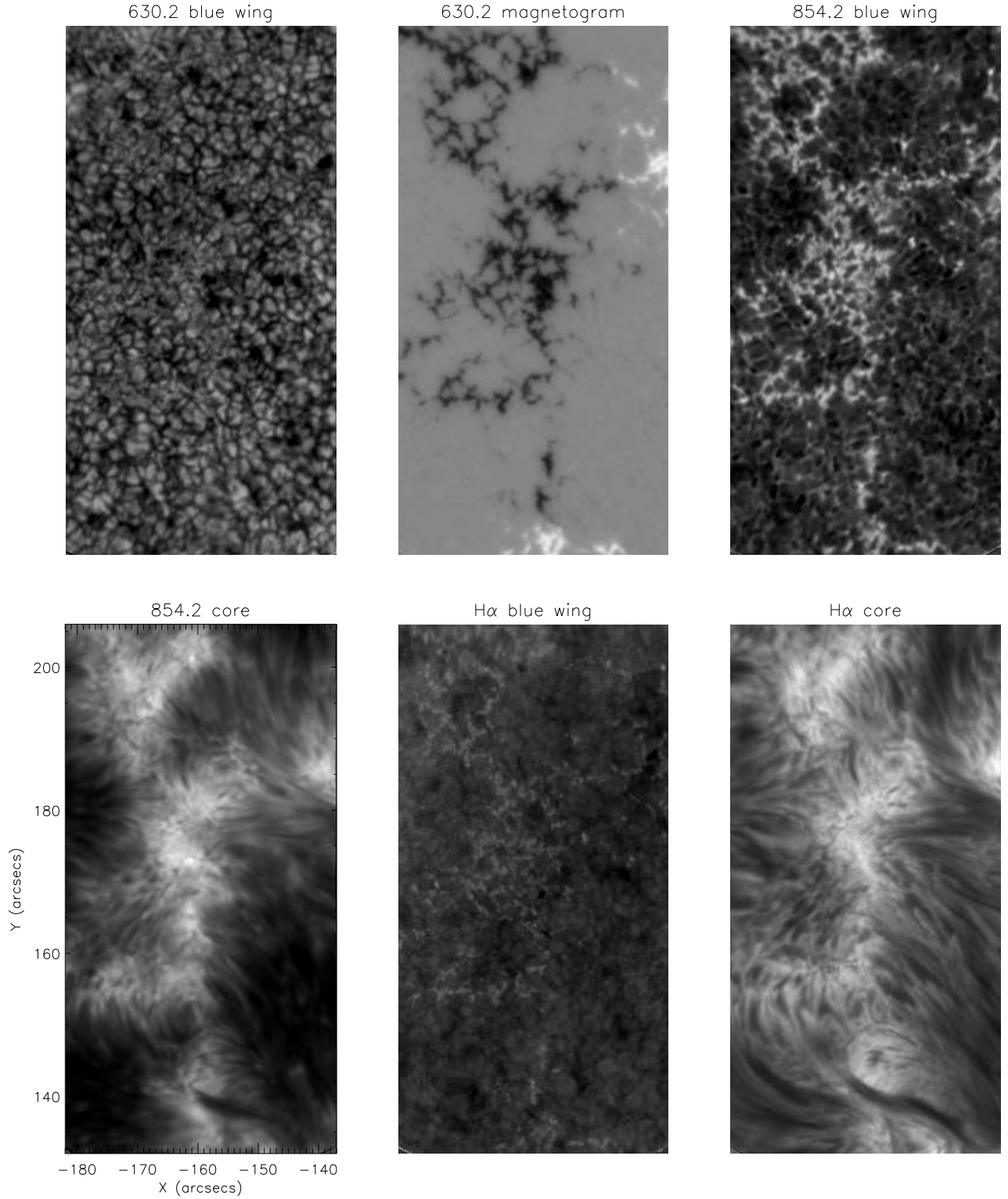


Figure 2. Typical IBIS data of NOAA 10996 observed on 20 May 2008 from scan number 11. Almost the entire IBIS FOV is shown. The “magnetogram” is simply $V(-74 \text{ m}\text{\AA})$ minus $V(+56 \text{ m}\text{\AA})$ for the Fe I line.

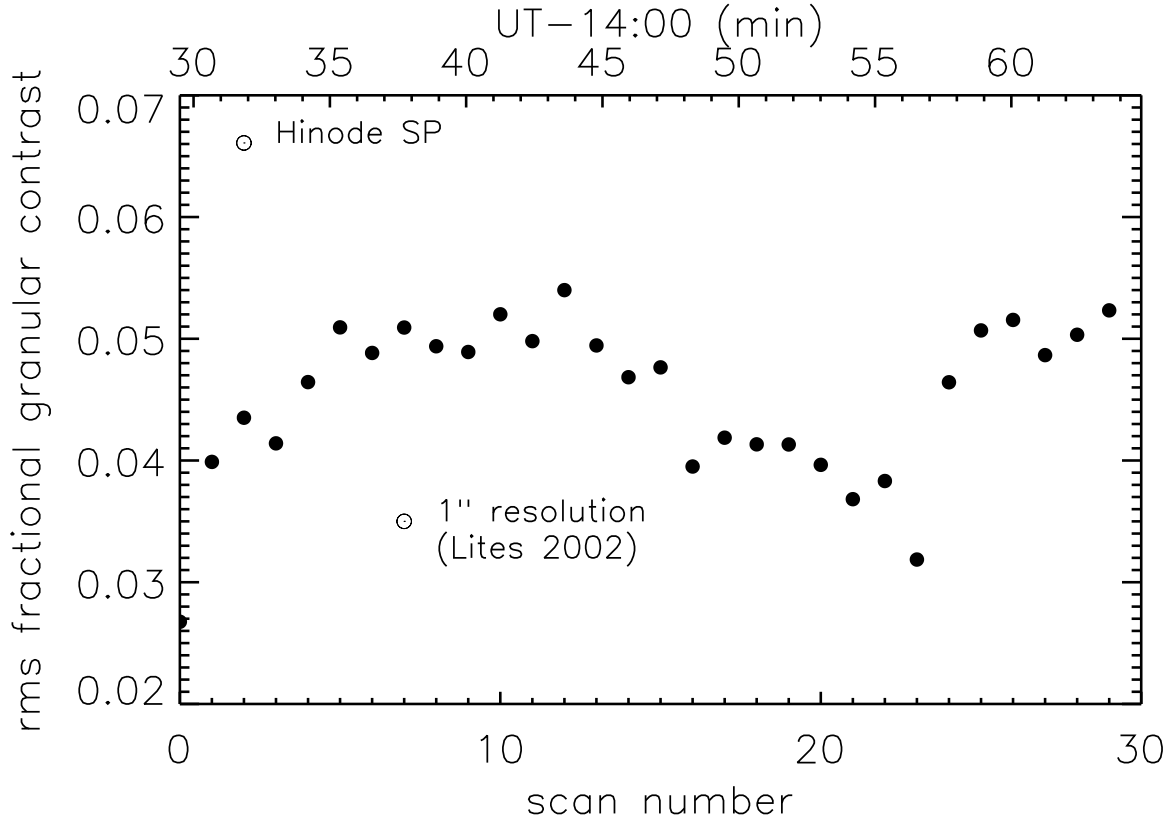


Figure 3. RMS granular contrasts are shown for the quietest regions of the IBIS and *Hinode* SP FOV, as measured in the continuum near 630.2 nm. Also shown is the contrast corresponding to an effective 1'' resolution derived by Lites (2002).

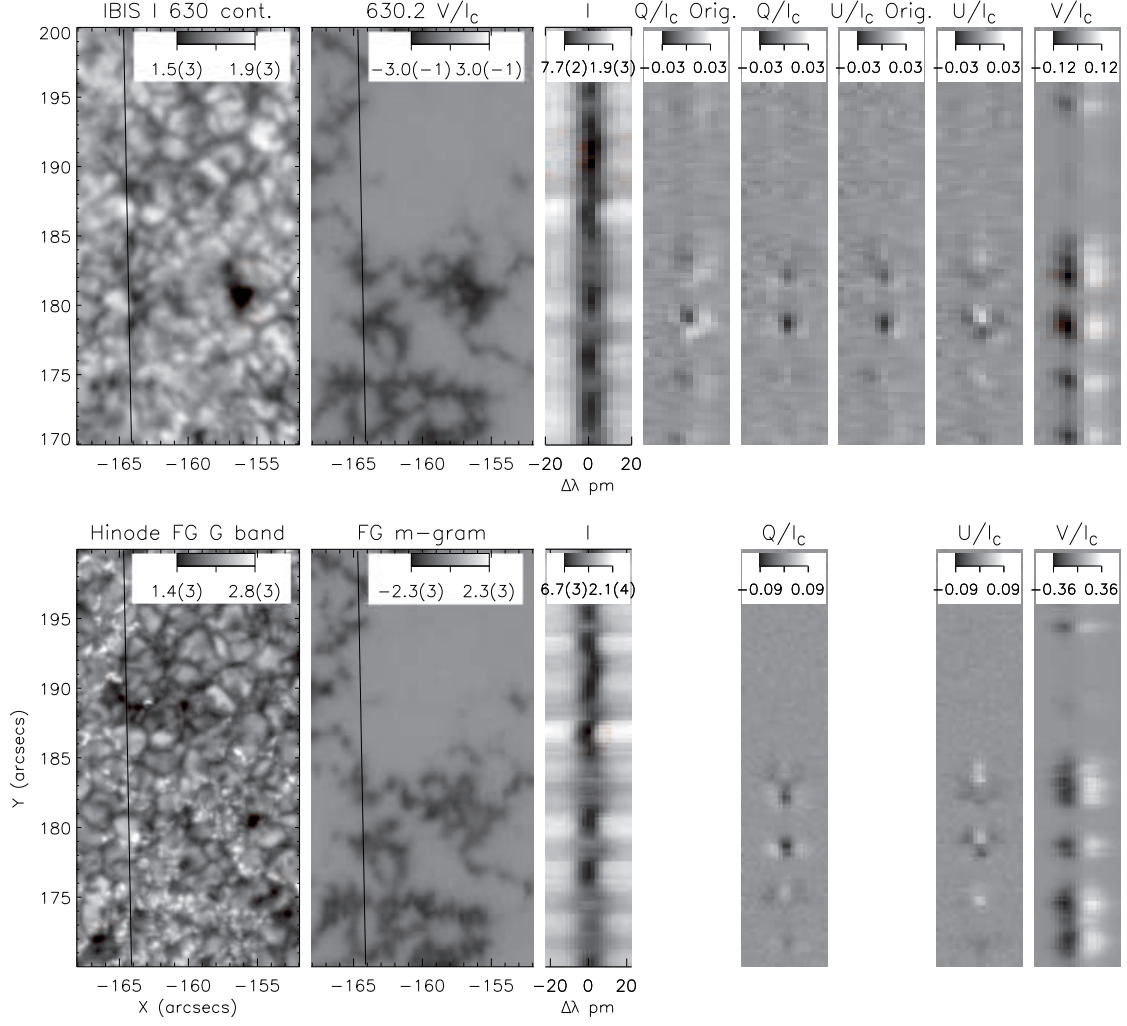


Figure 4. Typical IBIS and *Hinode* SP polarimetric measurements of the 630.2 nm line. The upper panels show IBIS data, the lower show *Hinode* data. The leftmost column shows intensity images, the next column magnetograms, from IBIS ($(V_{\lambda_0+6pm} - V_{\lambda_0-6pm})/I_C$, λ_0 = rest wavelength.) and the FG instrument on *Hinode* (in Mx cm^{-2}). The near-vertical line shows the position of the *Hinode* slit at 14:36:52 UT, from which the six rightmost images of Stokes profiles as a function of wavelength and position along the SP slit are taken. *QU* data marked “Orig.” are before subtraction of crosstalk and a final rotation in the polarization plane, the unflagged *QU* data include these corrections. IBIS profiles are extracted from the data closest in time and space to the SP measurements. Color scales are shown at the top of each image, where $x.y(z) \equiv x.y \times 10^z$.

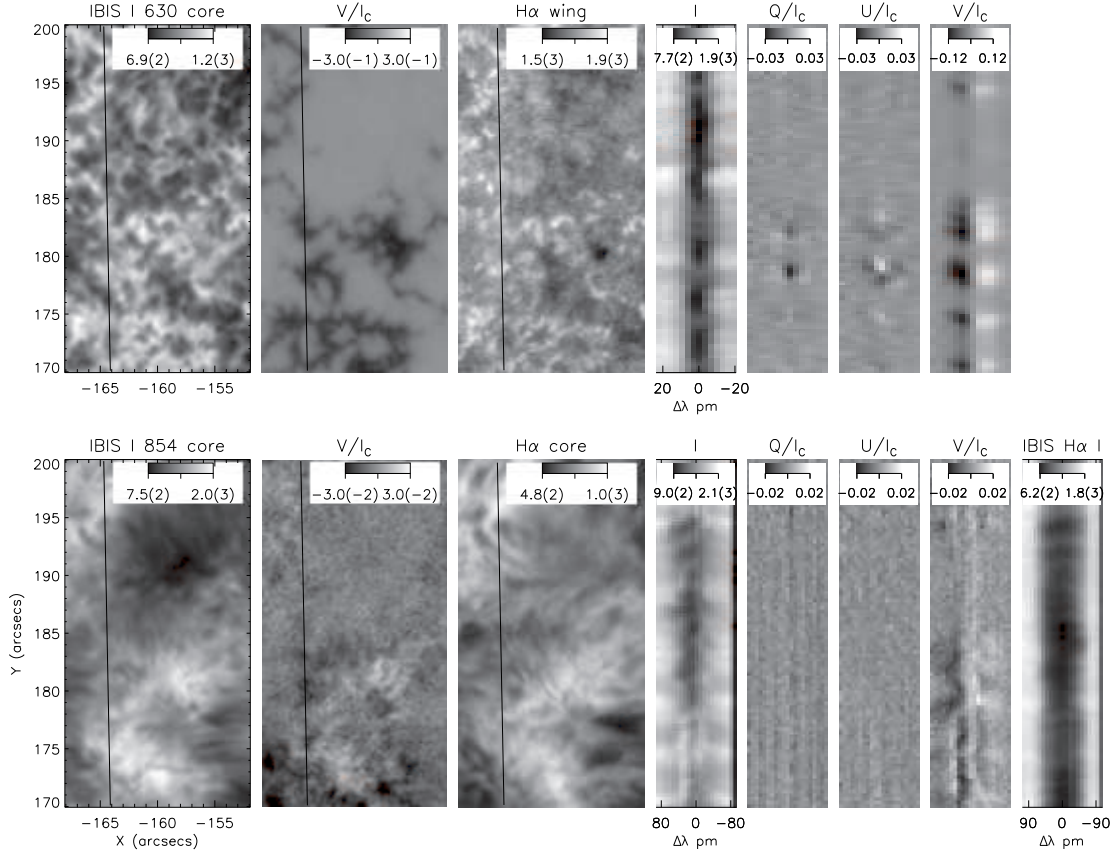


Figure 5. A figure similar to figure 4, except that the lower panels are IBIS data for the 854.2 nm line of Ca II and Hα, the V/I_C frame for Ca II shows $(V_{\lambda_0+17pm} - V_{\lambda_0-17pm})/I_C$.

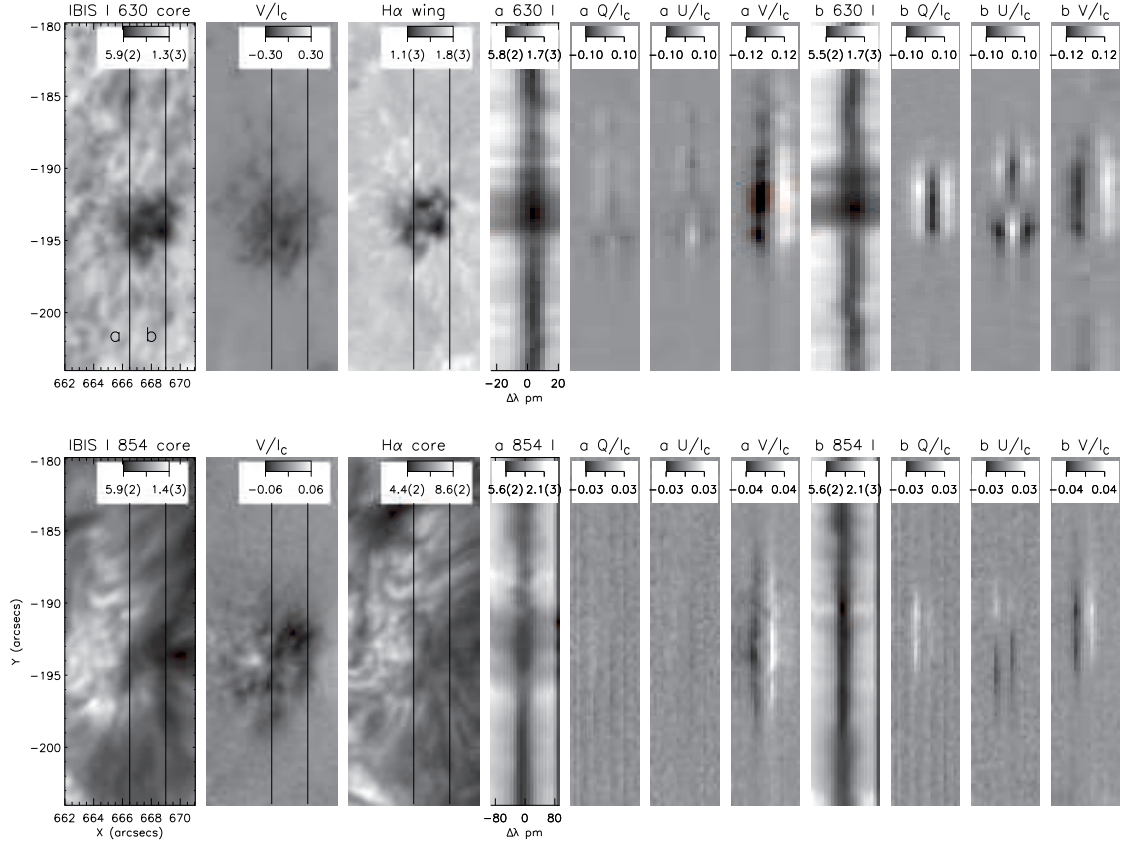


Figure 6. A figure similar to figure 4, showing the pore region associated with NOAA 10994 at S12.4, W46.1.

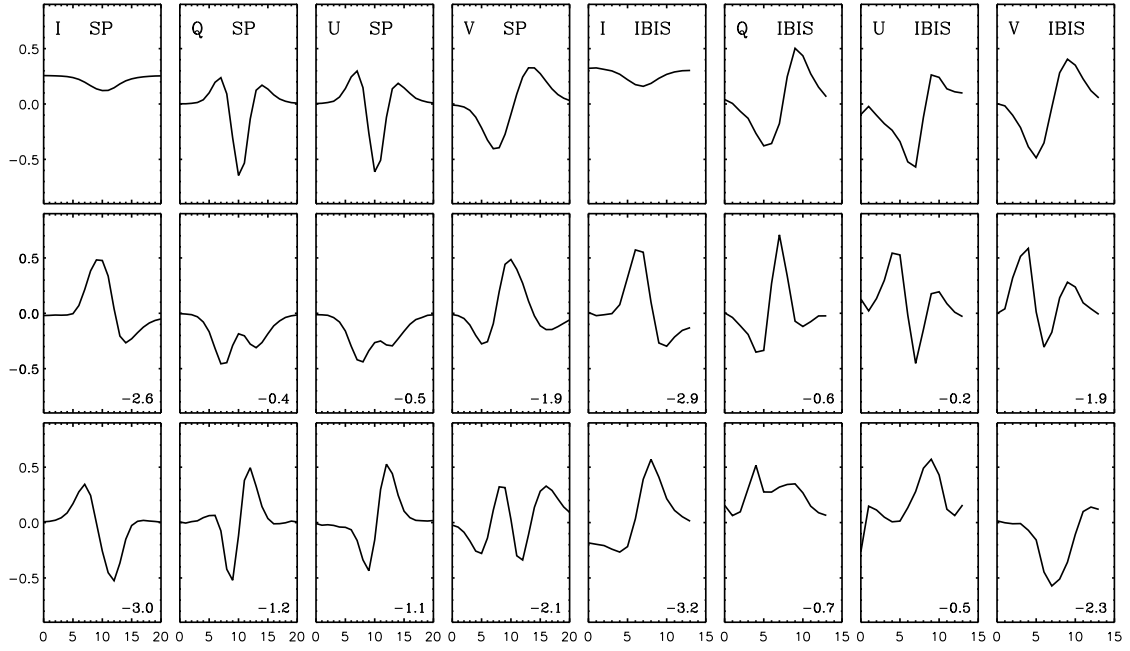


Figure 7. The first three eigenvectors in the PCA expansion for each of the four Stokes parameters of the Fe I 630.2 nm line are shown, for the IBIS data from 14:43 UT on 20 May 2008, and the corresponding *Hinode* SP data. The first row is the eigenvector with the largest eigenvalue, the second and third show the eigenvectors for the second and third largest eigenvalues. The second and third rows lists \log_{10} of the modulus of the eigenvalue (the largest is set to 1). The columns are labelled with the instrument and Stokes parameter. The abscissa is wavelength index.

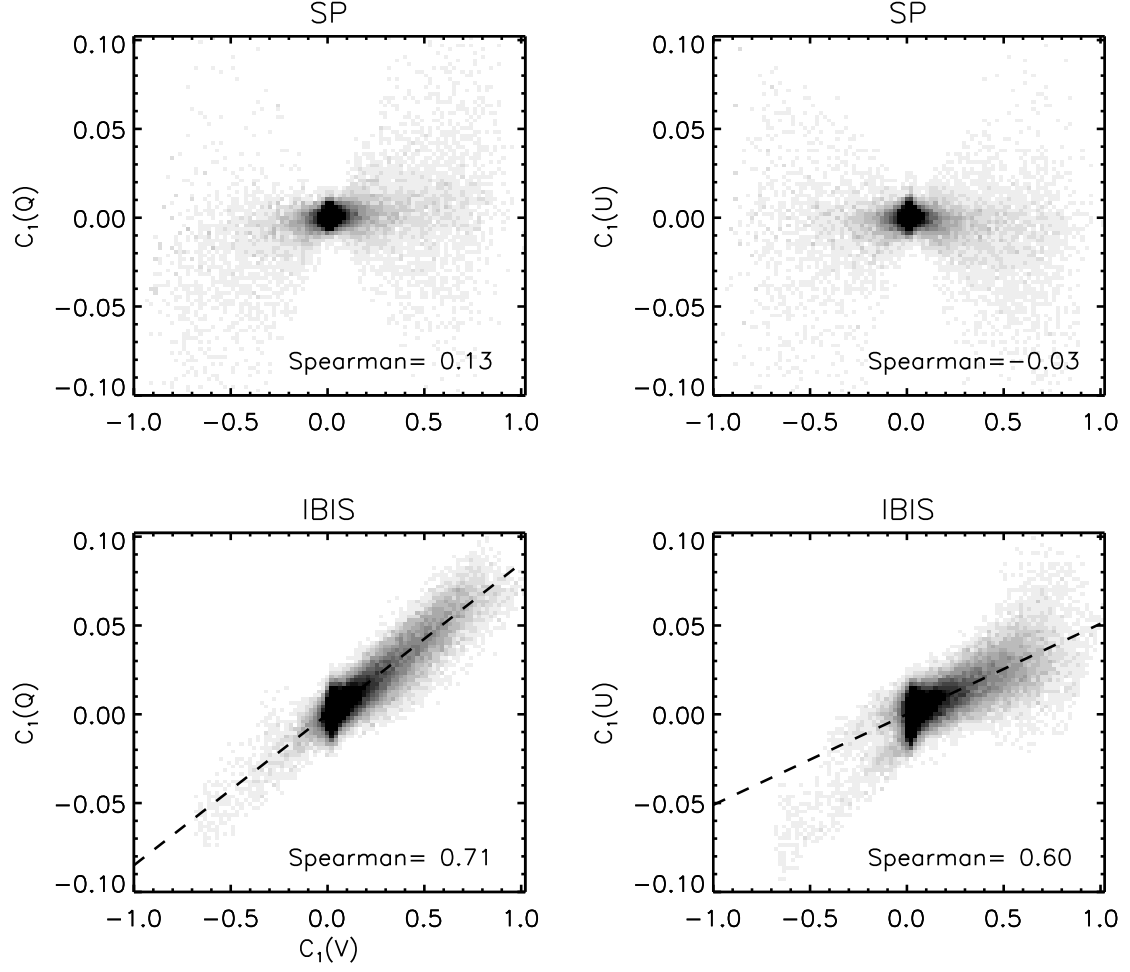


Figure 8. Scatter plot of the leading coefficients in the principal component expansion for Stokes QU and for V . The dashed lines show the relations $c_1(Q) = 0.085c_1(V)$ and $c_1(U) = 0.051c_1(V)$ derived empirically using the symmetry properties discussed in the text.

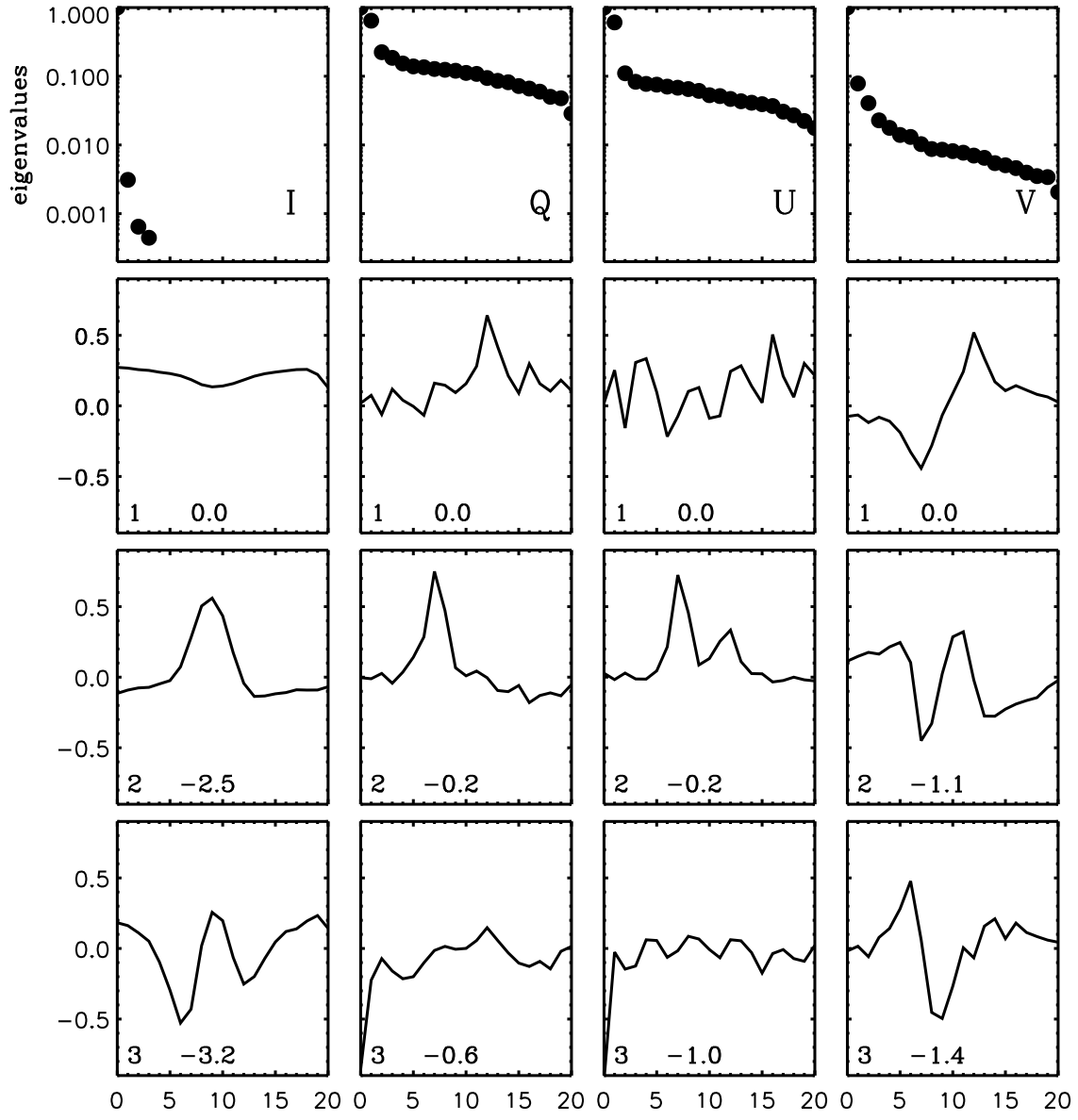


Figure 9. Eigenvalues and the first three eigenvectors from a PCA analysis of the 854.2nm line of Ca II. The data are constructed from the central $10'' \times 10''$ area of the pore, NOAA 10994, where significant linear polarization was measured.

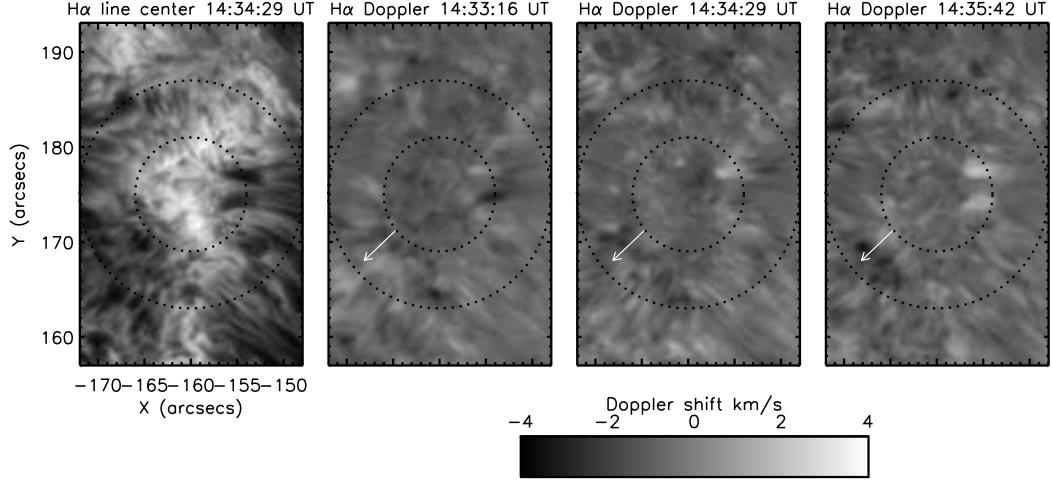


Figure 10. $H\alpha$ data shown for NOAA 10996. The leftmost image is a simple intensity image, the others show the time sequence of three snapshots taken roughly 70s apart, of Doppler shifts derived using the PCA technique. Bright features are redshifted, dark features blue shifted. The dark blobs near 8 o'clock (see the arrow) propagate roughly outwards from the centers of the circles marking a bright concentration of magnetic flux. These data are qualitatively compatible with magnetic field-directed flows along the magnetic fields originating from the flux concentration and expanding into the overlying corona. The velocity vectors can in principle yield the direction of the magnetic field.